PAPER

Check for updates

Hydration performance and optimization of multi-solid waste composite calcined sewage sludge

Juntao Ma,*[a] Hao Zheng, [ID] [a] Hao Qiu,[a] Yunfei Tan[b] and Shunbo Zhao[a]

The rapid increase in sewage sludge (SS) production and the global pursuit of carbon neutrality have driven the demand for the high-value construction material utilization of SS. In this study, calcium-rich solid wastes—carbide slag (CS) and phosphogypsum (PG)—were co-calcined with SS at elevated temperatures (800–1000 °C) to address the insufficient cementitious activity of thermally activated sludge. The resulting products were used to replace 30% of ordinary Portland cement (OPC) in pastes. The effects of calcination temperature, CS addition, and PG addition on the properties of calcined SS and its pastes were systematically investigated using XRD, FTIR, SEM, T_2NMR, and TG-DSC. Results showed that calcination at 800 °C converted kaolinite and muscovite in SS into amorphous reactive phases, significantly enhancing pozzolanic activity and mechanical strength. Co-calcination with CS and PG facilitated the formation of anorthite and calcium aluminate gels, further improving paste hydration (AFt, CH formation) and reducing its porosity. When CS and PG replaced 30% and 15% of SS, respectively, and the mixture was calcined at 800 °C, a clear synergistic hydration effect was observed. Response surface methodology identified the optimal conditions as 882.45 °C, 14.78% CS, and 2.62% PG, under which the compressive strength reached 85% of that of OPC, with a production cost of 190.19 RMB per t and carbon emissions of 529.17 kg CO_2 e per t, both notably reduced compared to OPC. These results demonstrate that MWCS is a promising sustainable cementitious material for low-strength engineering applications or as a partial cement replacement.

1 Introduction

Sewage sludge (SS), the principal solid byproduct of urban wastewater treatment, contains toxic substances, including heavy metals.[1–3] If not properly treated, SS can pose significant risks to human health and act as a potential source of secondary environmental pollution.[4–6] In China, SS has long encountered the dual challenges of high production and low utilization rates, while conventional disposal methods, such as landfill and incineration,[7] have led to serious environmental pollution and substantial resource wastage.[8,9] Over the past decades, researchers have actively explored the utilization of SS in construction materials, resulting in notable advancements. The feasibility of producing construction backfill materials[10,11] and pavement fillers[12,13] from SS has been demonstrated in numerous studies. However, with the growing emphasis on carbon neutrality, the low-carbon and high-value utilization of SS in the construction sector has emerged as a research focus. The application of SS has gradually shifted from low-value fillers to higher-value products, such as bricks[14–16] and cement

production.[17–19] Meanwhile, the pozzolanic activity potential of SS, attributed to its content of reactive inorganic components such as silicon and aluminum, has garnered increasing research attention. Consequently, SS has been increasingly recognized as a promising supplementary cementitious material (SCM) for the development of novel binders.[20–23]

The inherently low reactivity of SS presents a persistent challenge for its application as an SCM. High-temperature calcination, as a widely adopted thermal activation method, has been demonstrated to effectively enhance the pozzolanic activity of various aluminosilicate materials.[24–26] Accordingly, numerous studies have systematically investigated the effects and mechanisms of thermal activation on the reactivity of SS. For instance, Tantawy *et al.* reported that calcination at 600–900 °C facilitated the dehydration of $Al(OH)_3$ in SS, resulting in the formation of amorphous and reactive Al_2O_3 and silica gel, which are recognized as the principal contributors to the pozzolanic activity of SS. Their findings further indicated that calcination at 800 °C was sufficient to significantly enhance the reactivity of SS.[27] Similarly, another study examined the evolution of SS reactivity following calcination at 600–800 °C, demonstrating that increasing temperature promoted the dehydroxylation of crystalline silicon and aluminum, thereby generating highly reactive amorphous phases within this range.[28] Quantitative analysis by Chang *et al.* confirmed that the

[a]*International Joint Research Lab for Eco-building Materials and Engineering of Henan, North China University of Water Resources and Electric Power, Zhengzhou 450045, China. E-mail: majuntao@ncwu.edu.cn*

[b]*Zhengzhou Sewage Purification Co., Ltd, Zhengzhou 450045, China*

amorphous content in SS peaked at 800 °C, further substantiating the results of previous investigations.[29] Moreover, Fernandes *et al.* assessed the reactivity of SS by monitoring calcium hydroxide (CH) consumption after calcination at 600–800 °C. Their results showed that CH consumption declined with increasing calcination temperature, suggesting that an optimal temperature is required to maximize the activation of SS reactivity.[30] Although thermal activation has been shown to improve the pozzolanic activity of SS, the intrinsic lack of cementitious properties in thermally activated SS continues to restrict its widespread application. As a result, enhancing the cementitious properties of SS has emerged as a more promising research direction, since synergistic hydration with cement could broaden its application in low-carbon and high-value construction materials. Cementitious properties are primarily derived from the hydration of silicate minerals, such as C_2S and C_3S in Portland cement.[31] For SS rich in silicon and aluminum, the deficiency of calcium is generally regarded as the critical factor limiting its cementitious performance.

The synergistic co-utilization of multiple solid wastes has become a widely accepted strategy for enhancing the cementitious properties of waste-derived materials. At elevated temperatures, calcium, silicon, and aluminum sourced from different types of solid wastes can interact synergistically to form cementitious phases.[32,33] Numerous studies have demonstrated the effectiveness of multi-solid waste synergy under such conditions. For example, Sun *et al.*[34] examined the feasibility of producing cementitious materials by co-calcining coal gangue, carbide slag, steel slag, and gypsum at high temperatures. Their findings indicated that the co-calcined product exhibited the formation of hydraulically active C_2S and $C_4A_3\check{S}$ phases, and the 3 day heat of hydration was approximately 40% higher than that of ordinary Portland cement. In a similar vein, Duan *et al.*[35] investigated the synergistic behavior of fly ash-carbide slag-flue gas desulfurization gypsum systems, showing that, after high-temperature calcination, these systems could hydrate to form AFt and C–S–H phases, thus overcoming the inability of the individual raw materials to hydrate independently. Gu *et al.*[36] further explored the hydration mechanisms within such systems, demonstrating that variations in the Ca/Si ratio played a crucial role in the generation of C–S–H phases. Additional research has documented the successful synthesis of high-performance cementitious materials from mixtures of fly ash, carbide slag, and desulfurized gypsum through high-temperature calcination, achieving compressive strengths exceeding 70 MPa after 28 days of curing.[37,38]

In this study, carbide slag and phosphogypsum were individually co-calcined with SS at elevated temperatures. The hydration characteristics of the calcined sludge and its performance in cementitious pastes were systematically examined using X-ray diffraction (XRD), Fourier-transform infrared spectroscopy (FTIR), T_2 nuclear magnetic resonance (T_2NMR), scanning electron microscopy (SEM), and thermogravimetric-differential scanning calorimetry (TG-DSC). Response surface methodology was employed to optimize the mix design of multi-solid waste composite calcined sewage sludge (MWCS). The suitability of the optimized MWCS as a cementitious material was evaluated based on mechanical strength tests, as well as assessments of production cost and carbon emissions.

2 Materials and methods

This study addresses three primary objectives: (a) elucidating the effect of calcination temperature on the reactivity of SS and its performance in cementitious pastes; (b) investigating the influence of temperature and the additions of carbide slag and phosphogypsum on the hydration properties of calcined sludge and its blended pastes; and (c) optimizing the mix design of MWCS using response surface methodology.

2.1 Materials

The raw materials utilized in this study included SS collected from Zhengzhou Municipal Sewage Purification Company (Henan province), carbide slag (CS) supplied by Henan Haohua Yuhang Chemical Co., Ltd, phosphogypsum (PG) sourced from Enshi, Hubei province, and 42.5-grade ordinary Portland cement (OPC) provided by Henan Tianrui Cement Plant. With the exception of OPC, all raw materials were oven-dried and subsequently ground to a fine powder using an SM500 × 500 ball mill. The chemical compositions and phase compositions of the raw materials, determined by X-ray fluorescence (XRF) and X-ray diffraction (XRD), are summarized in Table 1 and Fig. 1, respectively. The main chemical constituents and phase of SS are SiO_2, Al_2O_3, and quartz. For CS, the dominant chemical and mineral components are CaO and portlandite, whereas PG
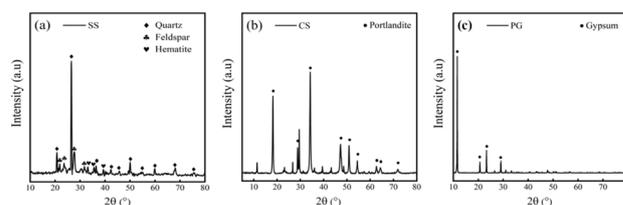

Fig. 1 Phase Composition of materials ((a) SS; (b) CS; (c) PG).

Table 1 Chemical composition of materials (mass%)

Materials	SiO_2	Al_2O_3	Fe_2O_3	CaO	MgO	SO_3	Na_2O	TiO_2	K_2O	P_2O_5	Loss
SS	38.97	11.71	4.09	3.44	2.11	3.69	1.12	0.47	2.15	—	31.92
CS	3.23	1.08	0.24	67.9	0.12	—	0.13	0.32	1.1	—	25.88
PG	3.19	0.57	1.25	38.25	0.18	48.98	0.13	1.1	0.08	1.19	3.88
OPC	22.36	4.15	2.59	60.13	2.17	1.95	0.79	—	—	—	5.37

Table 2 Performance of OPC

Apparent density (kg m^{-3})	Specific surface area (m^2 kg^{-1})	Setting time (min)		Compressive strength (MPa)		Flexural strength (MPa)	
		Initial	Final	3d	28d	3d	28d
3050	343	184	262	25.7	47.5	5.7	12.3

is primarily composed of SO$_3$, CaO, and gypsum. The physical properties of OPC are listed in Table 2.

2.2 Mix proportions

Calcination experiments were performed using an NBD-M 1700-30I tube furnace. The set temperatures (ST) were 800 °C, 900 °C, and 1000 °C. The furnace was initially heated from room temperature to 100 °C below the ST at a rate of 7 °C min^{-1}, followed by heating to the target ST at 3 °C min^{-1}, and subsequently held at the target temperature for 30 minutes. The calcination procedure is depicted in Fig. 2. The calcined SS was used to replace 30% of OPC in the preparation of cementitious pastes. The mix proportions for the calcined sludge and the

corresponding pastes are detailed in Table 3. Calcination temperature, CS addition, and PG addition were selected as independent variables, while the 3 day and 28 day compressive strengths of multi-solid waste composite sludge pastes were used as response variables. The Box–Behnken response surface methodology[39,40] was employed to optimize the multi-solid waste composite sludge mix proportions design. The factors and levels for the response surface design are summarized in Table 4.

2.3 Forming and testing methods

2.3.1. Method for forming paste samples. Calcined SS and OPC were mixed with water at a water-to-binder ratio of 0.4 to produce a homogeneous fresh paste, which was subsequently cast into 40 mm × 40 mm × 40 mm cubic molds and cured at room temperature for 24 hours. After demolding, the samples
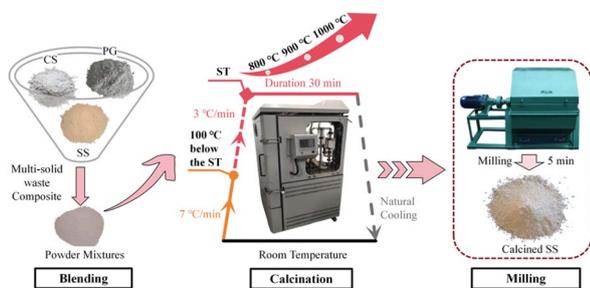

Fig. 2 Calcination process.

Table 4 Factors and levels of independent variables

Serials	Factors	Levels		
		−1	0	1
A	Temperature (°C)	800	900	1000
B	CS additions (%)	10	15	20
C	PG additions (%)	0	3	6

Table 3 Mix proportions of calcined SS and pastes

Paste groups	Water (g)	OPC (g)	SS (g)	Mix proportions for calcination of SS and multi-solid waste composite SS				
				Raw material group	SS (%)	CS (%)	PG (%)	Temperature (°C)
P-C	200	500	0	C	—	—	—	—
P-SS	200	350	150	SS	—	—	—	—
P-SS-800/900/1000	200	350	150	SS-800/900/1000	100	—	—	800
								900
								1000
P-SSxCS-800/900/1000	200	350	150	SSxCS-800/900/1000	95	5	—	800
	200	350	150		90	10	—	
	200	350	150		85	15	—	900
	200	350	150		80	20	—	
	200	350	150		75	25	—	1000
	200	350	150		70	30	—	
P-SSyPG-800/900/1000	200	350	150	SSyPG-800/900/1000	95	—	5	800
	200	350	150		90	—	10	
	200	350	150		85	—	15	900
	200	350	150		80	—	20	
	200	350	150		75	—	25	1000
	200	350	150		70	—	30	

Fig. 3 Forming method.

were further cured under standard conditions (20 ± 2 °C and $95 \pm 2\%$ relative humidity) for 3 days and 28 days, respectively. The preparation and curing procedure for the paste samples is depicted in Fig. 3.

2.3.2. Test methods. The 3 day and 28 day compressive strengths of the paste specimens were measured in accordance with GB/T 17671-1999, "Cement Mortar Strength Test Method (ISO Method)".[41] The pozzolanic and hydration activities of calcined SS, as well as its hydration performance in the paste, were characterized using a Bruker D8 ADVANCE X-ray diffractometer (XRD, scanning range: 10–80°), a Sigma 300 scanning electron microscope (SEM), a Nicolet iS10 Fourier-transform infrared spectrometer (FTIR, 400–4000 cm^{-1}), an NMI 20-015 V-I low-field nuclear magnetic resonance spectrometer (T$_2$NMR), and a Mettler TGA/DSC 3+ simultaneous thermal analyzer (TG-DSC, Switzerland).

3 Results

3.1 Effect of calcination temperature

3.1.1. SS reactivity. Fig. 4 illustrates the phase composition of SS before and after calcination at various temperatures. Prior to calcination, the principal potentially reactive minerals in SS are quartz (SiO$_2$), kaolinite (Al$_2$(Si$_2$O$_5$)(OH)$_4$), and muscovite (M, KAl$_2$(AlSi$_3$O$_{10}$)(OH)$_2$), while other minerals are considered inert.[42,43] Previous studies have reported that the pozzolanic reactivity of SS primarily arises from the transformation of kaolinite into amorphous phases during calcination,[44] however, due to the non-crystalline nature of amorphous phases, no corresponding diffraction peaks are observed.[45] Following calcination, the diffraction peak of quartz in SS shifts at 800 °C, which is attributed to the transformation from α-quartz to β-quartz.[30] The intensity of the muscovite diffraction peak

decreases with increasing temperature, reaching a minimum at 800 °C, primarily due to dehydration and dehydroxylation processes,[27,29] resulting in the decomposition of muscovite into reactive Al$_2$O$_3$ and SiO$_2$ at elevated temperatures. These observations indicate that the destruction of crystal structures at high temperatures facilitates the formation of amorphous phases, with 800 °C being the optimal temperature. This finding is consistent with the conclusions of Tantawy *et al.*.[27] Notably, a distinct mullite phase appears in SS after calcination, with its diffraction peak intensity increasing significantly at 900 °C and reaching a maximum at 1000 °C. Mullite is a stable crystalline phase formed from the transformation of silico- and aluminaminerals under high-temperature calcination,[46] suggesting that excessive temperatures may hinder the conversion from crystalline to amorphous phases.

Fig. 5 presents the FTIR spectra of SS before and after calcination at different temperatures. The absorption band observed at 3425 cm^{-1} in SS calcined at all three temperatures corresponds to the vibration of –O–H in structural water, with the largest peak area detected at 800 °C. This observation aligns with the variation in the muscovite diffraction peak in the XRD results, confirming that the most significant dehydration and dehydroxylation reactions occur at 800 °C. The asymmetric stretching vibration peaks of Si(Al^{IV})–O–Si in the 1000–1100 cm^{-1} region shift to higher wavenumbers and become broader, indicating that mineral dehydration reduces the interlayer spacing of silicate structures and decreases polyhedral crystallinity, thereby reflecting the impact of high-temperature calcination on the crystal structure. A new absorption band at 557 cm^{-1}, attributed to the vibration of Al–O–Si, appears after calcination, with its maximum area observed at 1000 °C, suggesting significant phase transformations at this temperature. This finding is consistent with the formation and evolution of the mullite phase identified in the XRD analysis. The Si–O vibration band around 464 cm^{-1} indicates changes in the SiO$_2$ crystal structure with increasing temperature.

Fig. 6 illustrates the microstructural evolution of SS before and after calcination at 800 °C (SS-800). The raw SS particles display irregular shapes, rough surfaces, and abundant pores, resulting in a loosely packed structure. In contrast, exposure to
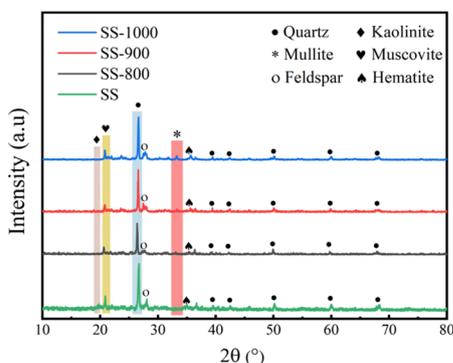

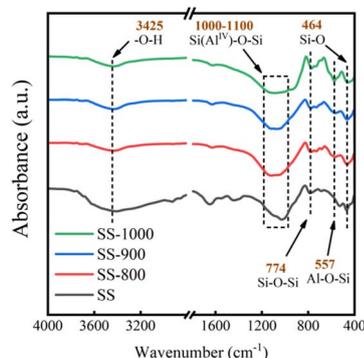**Fig. 4** Phase composition of SS at different calcination temperatures.

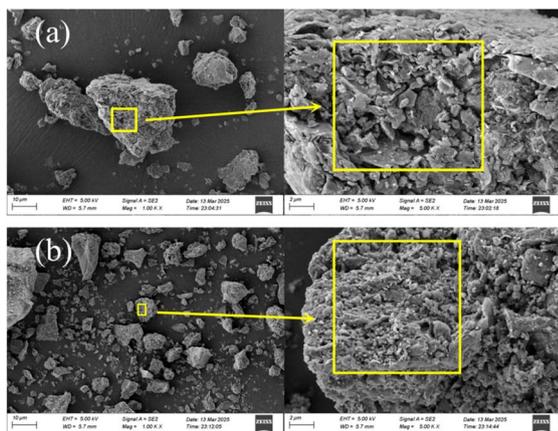**Fig. 5** FTIR results of SS at different calcination temperatures.

Fig. 6 Microstructure of SS before and after calcination ((a) SS; (b) SS-800).

Fig. 8 Phase composition of SS–OPC pastes with SS calcined at different temperatures ((a) 3 days; (b) 28 days).

high-temperature calcination induces pronounced morphological and structural modifications in SS. During calcination at 800 °C, mineral dehydration and dehydroxylation processes lead to more uniform particle morphology and smoother surfaces. Moreover, the disruption of crystalline structures and subsequent formation of amorphous phases contribute to the densification of the microstructure.

3.1.2. Paste properties. Fig. 7 displays the 3 day and 28 day compressive strengths of the pastes. With increasing curing age, all specimens exhibited a significant improvement in strength. Specifically, the 3 day and 28 day compressive strengths of the SS–OPC paste (P-SS) were 2.3 MPa and 24.0 MPa, respectively. In comparison, all calcined SS–OPC pastes demonstrated enhanced strengths, attributable to the additional hydration products generated by the pozzolanic reaction of calcined SS. Among these, the 3 day compressive strength of P-SS-900 was the highest, reaching 31.6 MPa, which corresponds to 86.1% of that of the pure cement paste (P-C). The highest 28 day compressive strength was observed for P-SS-800, at 62.8 MPa, corresponding to 93.5% of P-C. Considering the slow kinetics of the pozzolanic reaction, these results indicate that SS calcined at 800 °C exhibits the highest
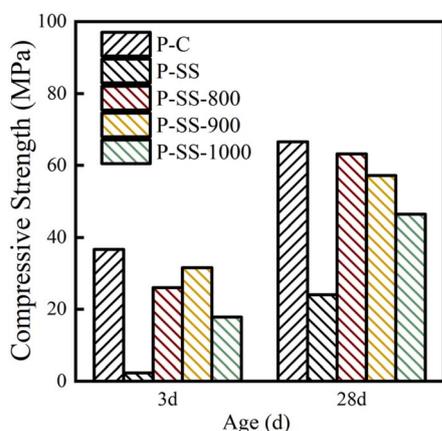
pozzolanic activity and is most conducive to the long-term strength development of the paste.

The phase composition of the pastes at 3 and 28 days was analyzed by XRD, and the results are presented in Fig. 8. Since the pozzolanic reaction consumes CH (portlandite),[47] changes in the intensity of the portlandite diffraction peaks can be used to evaluate the effect of SS calcined at different temperatures on the hydration behavior of the pastes. The results indicate that, compared to the OPC paste (P-C), the intensities of the CH diffraction peaks in the calcined SS–OPC pastes (P-SS-800/900/1000) were reduced at both 3 and 28 days, suggesting enhanced pozzolanic activity of the calcined SS. Notably, the CH peak intensities exhibited a more pronounced decrease at 28 days, implying a higher degree of pozzolanic reaction at this curing age. It is noteworthy that the lowest portlandite diffraction peak intensities at both 3 and 28 days were observed in the P-SS-800 paste, although the highest 3 day compressive strength was obtained for P-SS-900. This discrepancy can be attributed to the abundant formation of AFt (ettringite) in P-SS-900, which is known to positively influence early-age strength. Therefore, the high ettringite content in P-SS-900 accounts for its elevated 3 day strength. In contrast, the substantial reduction of portlandite in P-SS-800 indicates that SS calcined at 800 °C underwent the most effective pozzolanic reaction, resulting in greater CH consumption. These findings further confirm that calcination at 800 °C is sufficient to activate the pozzolanic reactivity of SS.
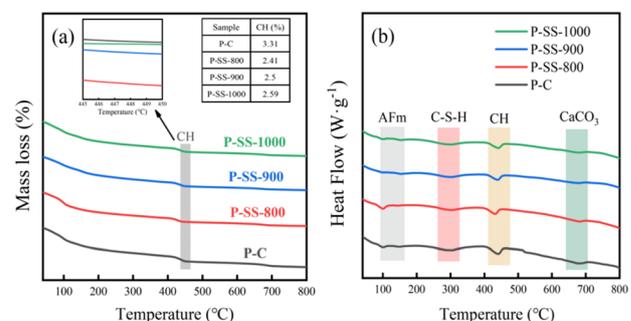

Fig. 7 XRD patterns of samples with different GSGS and GCS ratios.

Fig. 9 TG-DSC results of 28 day SS–OPC pastes with SS calcined at different temperatures ((a) TG; (b) DSC).

Paper

To corroborate the XRD results, phase changes and the quantitative analysis of CH in the 28 day pastes were further investigated by TG-DSC, as shown in Fig. 9. The TG curve represents the mass loss associated with mineral decomposition, while the DSC curve reflects the corresponding heat flow. Typically, the decomposition of minerals such as C–S–H, AFt, and AFm occurs below 400 °C.[48] The mass loss observed between 400 °C and 500 °C is primarily attributed to the dehydration of CH.[49] Compared with P-C, the incorporation of calcined SS led to only minor changes in the endothermic peak of CH, which is consistent with the variations in the portlandite diffraction peaks observed in the XRD results, indicating a limited reaction between calcined SS and CH. The DSC data further confirmed the limited pozzolanic reactivity of the calcined SS. Quantitative analysis revealed that the CH contents in the P-C, P-SS-800, P-SS-900, and P-SS-1000 pastes were 3.31%, 2.41%, 2.5%, and 2.59%, respectively, indicating that the pozzolanic reaction of SS calcined at 800 °C was the most significant.

Fig. 10 presents the pore structure of the 28 day pastes as characterized by T_2NMR. T_2NMR facilitates the analysis of pore size distribution during the hydration process by measuring relaxation times.[50] The spectra exhibit two principal peaks: the primary peak centered at approximately 6 ms and the secondary peak at around 30 ms, corresponding to large and small pores, respectively. The relative heights of the primary peaks for the four pastes are ranked as follows: P-SS-800 > P-SS-1000 > P-C > P-SS-900, indicating differences in small pore distribution and the influence of calcination temperature on the pore structure of SS–OPC pastes. Further analysis, using P-C as the control, revealed that for P-SS-800, the area of the primary peak decreased while the secondary peak remained unchanged, and both peaks shifted towards shorter relaxation times. This suggests that SS calcined at 800 °C reduced both the pore size and overall porosity of the paste. For P-SS-900, both the primary and secondary peak areas remained largely unchanged, but both peaks shifted slightly towards shorter relaxation times, indicating that the incorporation of SS calcined at 900 °C resulted in the transformation of some large pores into small
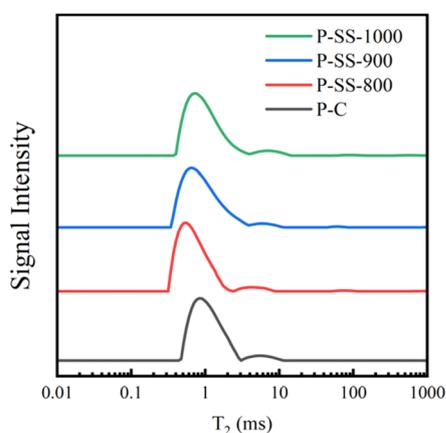
pores and promoted a more uniform pore size distribution, without markedly affecting total porosity. In contrast, for P-SS-1000, although the primary peak area showed minimal change, the secondary peak area increased slightly, and both peaks shifted towards longer relaxation times, indicating that SS calcined at 1000 °C increased both the pore size and porosity of the paste.

3.2 Effect of CS/PG addition at different calcination temperatures

3.2.1. Paste compressive strength. Fig. 11 illustrates the variations in compressive strength of calcined SS–OPC pastes with different CS and PG additions at various calcination temperatures. At 3 days, increasing the CS addition enhances strength at both 800 °C and 1000 °C, with the maximum values observed at 25% CS (32.1 MPa) and 30% CS (26.6 MPa), respectively. In contrast, at 900 °C, a local strength maximum (30.3 MPa) occurs at 15% CS, although it remains lower than that of the paste without CS addition (Fig. 11a), indicating an interaction effect between temperature and CS addition. At 28 days, only at 800 °C and 1000 °C do the strengths at 5% and 30% CS, respectively, slightly exceed those of the controls, while at 900 °C, the strength consistently remains lower (Fig. 11b). These results demonstrate that the maximum compressive strengths at 3 and 28 days were achieved by P-SS25CS-800 and P-SS5CS-800, respectively. This suggests that early-age strength enhancement is favored by calcination at 800 °C with a higher CS addition (25%), whereas long-term strength is more closely associated with a lower CS addition (5%) at 800 °C.

For pastes containing PG, the 3 day compressive strength at both 800 °C and 1000 °C initially increases and then decreases with increasing PG addition, reaching maxima at 5% (27.9 MPa) and 15% (20.5 MPa), respectively. At 900 °C, the strength
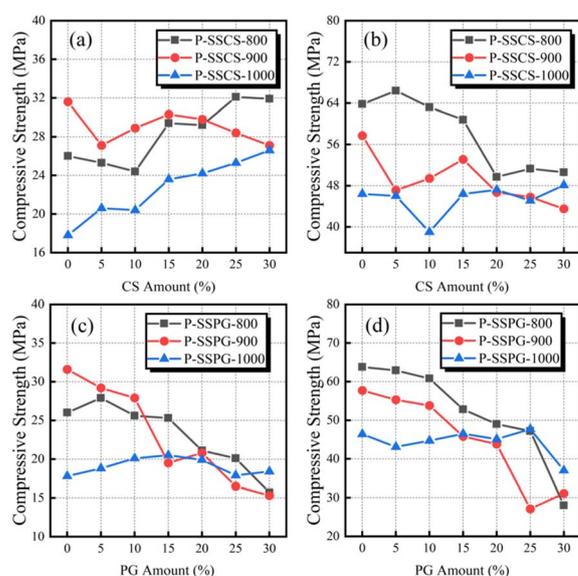

Fig. 10 T_2NMR results of 28 day SS–OPC pastes with SS calcined at different temperatures.

Fig. 11 Compressive strength of calcined SS–OPC pastes with varying CS/PG additions (a) CS 3 days; (b) CS 28 days; (c) PG 3 days; (d) PG 28 days.

demonstrates a trend of gradual decline, sharp drop, and fluctuation, with a local maximum (27.9 MPa) at 10% PG, but still lower than the control (Fig. 11c). At 28 days, only the P-SS25PG-1000 sample (47.7 MPa) exhibited higher strength than the control, while no significant changes were observed in the other samples (Fig. 11d). Thus, the highest 3 day and 28 day compressive strengths for PG-incorporated calcined SS–OPC pastes were observed in P-SS5PG-800 and P-SS25PG-1000, respectively. These findings suggest that the effect of PG addition is temperature-dependent: early-age strength enhancement is more readily achieved at 800 °C with a lower PG addition (5%), while long-term strength relies on the combination of 1000 °C and a higher PG addition (25%). Notably, the 28 day strengths of pastes calcined at 800 °C with low PG additions (<10%) were the highest among all samples.

3.2.2. Hydration properties of SS. XRD analysis was conducted to characterize the phase composition of SS calcined at different temperatures with the addition of 10%, 20%, and 30% CS or 5%, 10%, and 15% PG, and the results were compared with those of raw SS. As shown in Fig. 12, the mineral composition of SS was consistent with the findings in Section 3.1.1, being predominantly composed of quartz, kaolinite, muscovite, and other potentially reactive or inert minerals. After calcination, certain active phases were formed, along with the emergence of mullite. Distinct from the unblended samples, those containing CS exhibited the formation of anorthite ($CaAl_2Si_2O_8$) and CA ($CaO \cdot Al_2O_3$) phases at all temperatures, resulting from the synergistic reaction of SiO_2 and Al_2O_3 (from the decomposition of muscovite and kaolinite) with Ca from CS at high temperature.[44] Additionally, amorphous $Al(OH)_3$ generated during phase transformation can react with $CaCO_3$ to produce CA.[51] The effect of CS addition showed that cementitious phases at a low CS addition (10%) were more concentrated in SS calcined at 900 °C, whereas higher CS additions (20% and 30%) favored their formation at 800 °C. This finding confirms the interactive effect between calcination temperature and CS addition. Given that excessively high temperatures adversely affect the reactivity of SS, a CS addition of 30% combined with calcination at 800 °C is considered more favorable for developing the cementitious properties of SS.
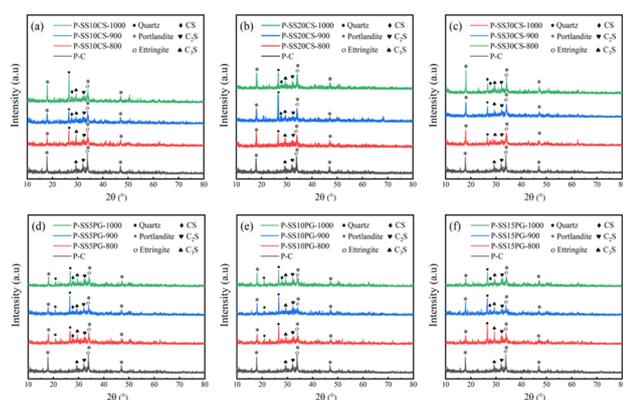
For samples with PG addition, anorthite and CA phases were detected at all temperatures, and their diffraction peak intensities increased with higher PG addition, indicating that PG promoted anorthite formation at elevated temperatures.[52–54] This further demonstrates the interaction between temperature and PG addition. Moreover, CaO generated from the decomposition of PG at high temperatures, in combination with Al_2O_3, facilitated CA formation. The cementitious phases for all PG additions appeared most prominently in SS calcined at 800 °C, suggesting that this temperature is optimal for the decomposition and recombination of PG and SS minerals, thereby enhancing the cementitious properties of the calcined product.

The phase transformations of SS calcined with 30% CS addition or 15% PG addition at different temperatures were analyzed by FTIR to validate the XRD results. As shown in Fig. 13a, for SS calcined with 30% CS addition, the absorption peak at 3641 cm^{-1} is attributed to the dehydroxylation of kaolinite and its conversion into highly active metakaolinite.[44] The increased area of the CO_3^{2-} absorption peak at 1439 cm^{-1} indicates that CS decomposes at high temperature to form $CaCO_3$, which, together with $Al(OH)_3$, serves as a precursor for CA formation.[52] This observation aligns with the XRD findings. The increased areas of the Si–O–Si stretching vibration peaks at 1000–1100 cm^{-1} and 774 cm^{-1} after calcination with CS indicate that the introduction of Ca^{2+} promotes the transformation of silicate mineral structures into amorphous phases. In contrast, the pronounced reduction in the areas of the Al–O–Si and Si–O bending vibration peaks at 557 cm^{-1} and 464 cm^{-1} reveals the transformation of the quartz crystal structure.

For SS calcined with 15% PG addition, the absorption peaks in the 1500–3000 cm^{-1} range disappeared, a trend similar to that of SS calcined without PG (Fig. 13b). The changes in the Si–O–Si stretching peaks at 1000–1100 cm^{-1} and 774 cm^{-1} are also attributed to the breakdown of the crystal structure at high temperatures and the formation of amorphous aluminosilicates. However, the peak area increased and was accompanied by a shift in wavenumber for the PG-added sample, indicating that Ca^{2+} and SO_4^{2-} generated from the decomposition of PG promoted the polymerization of silicate minerals, resulting in the formation of calcium sulfoaluminate structures.[55] The appearance of S–O bending vibration peaks at 678 cm^{-1} and 602 cm^{-1} further confirms the contribution of PG to the formation of sulfate-containing structures. Unlike the results

Fig. 12 Phase composition of calcined SS with different CS/PG additions ((a) 10% CS; (b) 20% CS; (c) 30% CS; (d) 5% PG; (e) 10% PG; (f) 15% PG).
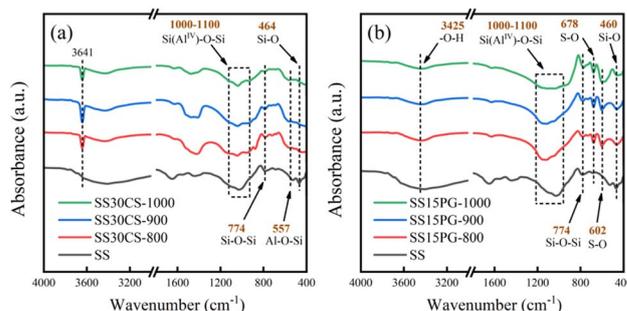

Fig. 13 FTIR results of calcined SS ((a) 30% CS; (b) 15% PG).
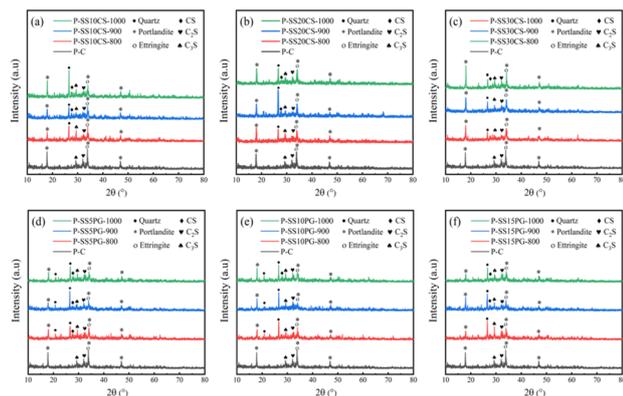
Fig. 14 Phase composition of 3 day calcined SS–OPC pastes with different CS/PG additions ((a) 10% CS; (b) 20% CS; (c) 30% CS; (d) 5% PG; (e) 10% PG; (f) 15% PG).

for CS addition, the reappearance of the Si–O bending peak at 460 cm^{-1} suggests that PG addition during calcination doesn't significantly affect the crystal structure of quartz in SS.

3.2.3. Paste hydration properties. Fig. 14 presents the 3 day phase composition results of calcined SS–OPC pastes containing 10%, 20%, and 30% CS or 5%, 10%, and 15% PG at different temperatures. Compared to P-C, the interaction between calcination temperature and addition significantly influenced the intensity of the portlandite diffraction peak. With 10% CS, the portlandite peak intensity increased with temperature but remained lower than that of P-C, reflecting the ongoing pozzolanic reaction. For 20% and 30% CS, portlandite peaks exceeding that of P-C were observed at 1000 °C and 800 °C, respectively, indicating more complete decomposition of the calcium source at higher temperatures. CS decomposes to CaO at 600–1000 °C,[56] which can either hydrate directly to form CH or react to generate C_2S and C_3S, which subsequently hydrate to produce CH. Thus, the increase in CH content may arise from multiple reaction pathways. However, this increase in CH content doesn't fully explain the strength development in the paste. The XRD results revealed that the lowest quartz peaks and the strongest AFt peaks for CS-blended pastes were concentrated at 800 °C, particularly at 30% CS, indicating that crystalline phase transformation was most pronounced at this temperature, facilitating the formation of reactive silica, alumina, CA, and AFt.

For 3 day pastes with PG addition, characteristic AFt peaks were enhanced at all temperatures, attributable to the reaction between SO_4^{2-} released from the thermal decomposition of PG and the aluminum source, which promotes AFt formation[57] and is accompanied by CH consumption.[58] At 800 °C, the intensity of the portlandite diffraction peak gradually decreased with increasing PG addition, further supporting this reaction mechanism. In contrast, at 900 °C and 1000 °C, the portlandite peaks first increased and then decreased, respectively, indicating that the reaction pathways of PG may vary with temperature. Further analysis showed that the thermal decomposition of PG also influences the formation of C_2S among the hydration products. The °C released from PG can delay the transformation

of C_2S to inert γ-C_2S,[59] while enhancing the hydration activity of C_2S.[60] The trend of the C_2S diffraction peak intensity was consistent with that of portlandite, confirming the synergistic effect of PG on the generation and hydration of C_2S at different temperatures. Therefore, calcined SS with PG addition exhibited reaction characteristics similar to those observed in the CS-blended samples.

Fig. 15 presents the 28 day phase composition results of calcined SS–OPC pastes with 10%, 20%, and 30% CS or 5%, 10%, and 15% PG at different temperatures. The overall trends are generally consistent with those observed at 3 days. Notably, the sample containing 20% CS at 800 °C (P-SS20CS-800) exhibited substantially lower portlandite and quartz diffraction peak intensities than other groups, indicating that the combination of 800 °C and this CS addition is favorable for crystalline phase reactions and structural transformation. Meanwhile, the intensity of the AFt phase showed no significant difference between the 20% and 30% CS samples, suggesting that the early-stage influence of CA-generated AFt diminishes over time, while secondary hydration driven by pozzolanic reactions becomes more prominent at later ages.[61] These results indicate that calcination at 800 °C with 20% CS addition is conducive to the long-term hydration reaction of the paste.

For the PG-incorporated pastes, the XRD results showed that at 800 °C, the portlandite peak intensity initially decreased and then increased with increasing PG addition, whereas at 900 °C and 1000 °C, the intensity first increased and then decreased. This variation suggests that PG addition affects the hydration reaction process at different temperatures. At elevated temperatures, the synergistic calcination of PG and SS enhanced the reactivity of C_2S, thereby promoting the later-stage formation of CH. Thus, the diffraction peak intensities of C_2S and CH can be used to evaluate the late hydration performance. The results revealed that for all three PG additions, the intensities of the portlandite and C_2S peaks followed the order 900 °C > 1000 °C > 800 °C, and for the 15% PG samples, the portlandite peaks were the most pronounced at each temperature, indicating that this addition favors the pozzolanic reaction and the late hydration of C_2S.
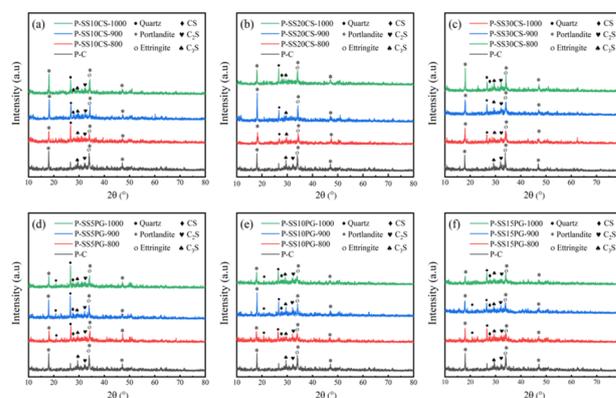

Fig. 15 Phase composition of 28 day calcined SS–OPC pastes with different CS/PG additions ((a) 10% CS; (b) 20% CS; (c) 30% CS; (d) 5% PG; (e) 10% PG; (f) 15% PG).
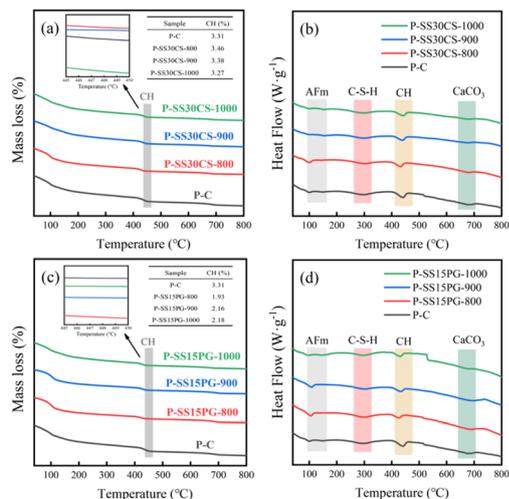
Fig. 16 TG-DSC results of 28 day calcined SS–OPC pastes ((a) 30% CS TG; (b) 30% CS DSC; (c) 15% PG TG; (d) 15% PG DSC).

Fig. 16 shows the 28 day TG-DSC results for calcined SS–OPC pastes containing 30% CS addition or 15% PG addition at different temperatures. The CH mass loss data indicate that, for the 800 °C group, the value is slightly higher than that of P-C, remains unchanged at 900 °C, and is slightly lower at 1000 °C, suggesting that, across different calcination temperatures, the incorporation of calcined SS with 30% CS addition doesn't inhibit the hydration of OPC. In the DSC curves, the thermal effects associated with AFm and C–S–H are also more pronounced in the 800 °C sample, indicating a synergistic enhancement of hydration. Quantitative analysis revealed that the CH contents of P-C, P-SS30CS-800, P-SS30CS-900, and P-SS30CS-1000 were 3.31%, 3.46%, 3.38%, and 3.27%, respectively. The slight increase in CH content may be attributed to the hydration of C_2S and C_3S produced from calcined CS.

For pastes containing 15% PG addition, the TG-DSC curves for all samples displayed decomposition peaks for AFm, confirming that PG provided a sulfur source during hydration and promoted AFm formation, consistent with the XRD results. Among the different calcination temperatures, P-SS15PG-800 exhibited the most significant mass loss and heat flow associated with AFm and C–S–H, indicating higher hydration activity at 800 °C. The CH content was significantly lower than that of P-C, with values for the four groups being 3.31%, 1.93%, 2.16%, and 2.18%, respectively, reflecting the consumption of CH during prolonged pozzolanic and hydration reactions.

Fig. 17 displays the T_2NMR pore structure characteristics of 28 day calcined SS–OPC pastes containing 30% CS addition or 15% PG addition at different calcination temperatures. As shown in Fig. 17a, for pastes with 30% CS addition, the main peak heights follow the order: P-SS30CS-1000 > P-SS30CS-900 > P-SS30CS-800. Compared to P-C, the primary and secondary peaks of P-SS30CS-800 become lower and broader and shift toward shorter relaxation times, with a slight decrease in the primary peak area and little change in the secondary peak. This indicates that SS calcined at 800 °C reduces pore size and decreases porosity. For the 900 °C sample, the primary peak
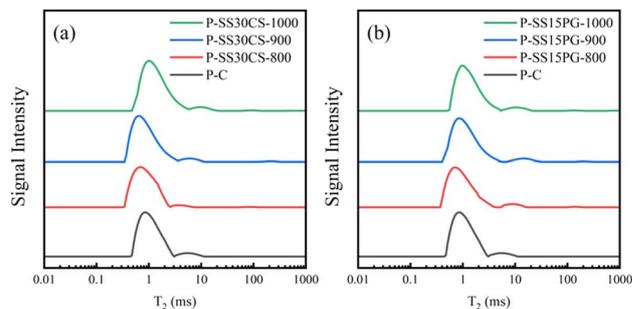

Fig. 17 T_2NMR results of 28 day calcined SS–OPC pastes with 30% CS/15% PG ((a) 30% CS; (b) 15% PG).

area increases slightly with a slight shift, and the secondary peak remains relatively unchanged, suggesting a reduction in small pore size while overall porosity remains stable. For the 1000 °C sample, both primary and secondary peak areas increase and shift toward longer relaxation times, indicating an overall increase in pore size and porosity.

For pastes with 15% PG addition, the main peak heights are ranked as P-SS15PG-1000 > P-SS15PG-900 > P-SS15PG-800. Compared to P-C, the primary and secondary peaks of the 800 °C sample become narrower and smaller, with the primary peak shifting toward shorter relaxation times and the secondary peak shifting toward longer relaxation times, indicating an increase in large pore size, a reduction in small pore size, and an overall decrease in porosity. In the 900 °C sample, the shapes of both peaks remain essentially stable, with only the secondary peak shifting, reflecting a slight increase in large pore size while the structure of small pores is maintained. In the 1000 °C sample, the primary peak increases in height and area, while the secondary peak becomes narrower and smaller, both shifting toward longer relaxation times, indicating a significant increase in both pore size and porosity.

3.3 MWCS optimization design

The optimization of MWCS was performed using response surface methodology for the paste specimens, as described in Section 2.2. The corresponding mix proportions and experimental results are presented in Table 5. The interactive effects of multiple factors were evaluated using 3D response surface plots and contour plots.[62,63] The slope of the 3D surface and the density of the contour lines both indicate the strength of the interactions between the influencing factors and the response variables.[64,65]

3.3.1. 3 day compressive strength. Table 6 presents the ANOVA results for the response values of the 3 day compressive strength model. Calcination temperature ($F = 77.39$) exerted the greatest influence on 3 day compressive strength, followed by PG addition ($F = 21.92$), whereas CS addition ($F = 3.95$) had the least effect. The p-values for calcination temperature and PG addition were both less than 0.05, indicating statistically significant effects on 3 day compressive strength.

Fig. 18 illustrates the interactive effects of multiple variables on 3 day compressive strength. The interaction between

Table 5 Response surface mix proportions and results

Std	Run	A: temperature (°C)	B: CS addition (%)	C: PG addition (%)	3 day compressive strength (MPa)	28 day compressive strength (MPa)
5	1	800	15	0	27.59	58.50
11	2	900	10	6	25.16	55.15
6	3	1000	15	0	24.64	50.84
4	4	1000	20	3	21.97	47.53
2	5	1000	10	3	21.66	56.14
8	6	1000	15	6	21.99	53.36
17	7	900	15	3	32.79	49.58
16	8	900	15	3	33.32	50.32
1	9	800	10	3	26.26	54.16
12	10	900	20	6	24.32	52.71
15	11	900	15	3	33.30	50.24
10	12	900	20	0	28.88	52.61
14	13	900	15	3	32.88	51.17
3	14	800	20	3	23.87	57.92
9	15	900	10	0	28.91	51.72
7	16	800	15	6	28.60	55.25
13	17	900	15	3	32.05	50.15

Table 6 ANOVA analysis of 3d compressive strength model of response value

Source	Sum of squares	Degrees of freedom	Mean square	F-value	P-value	Significance
Model	274.64	9	30.52	110.77	<0.0001	Highly significant
A	21.32	1	21.32	77.39	<0.0001	Highly significant
B	1.09	1	1.09	3.95	0.0873	Not significant
C	6.04	1	6.04	21.92	0.0023	Highly significant
AB	1.82	1	1.82	6.62	0.0369	Significant
AC	11.09	1	11.09	40.25	0.0004	Highly significant
BC	0.164	1	0.164	0.5954	0.4656	Not significant
A^2	72.35	1	72.35	262.63	<0.0001	Highly significant
B^2	117.51	1	117.51	426.55	<0.0001	Highly significant

calcination temperature and CS addition is characterized by a steep 3D response surface and dense contour lines, signifying a pronounced effect on the response variable (3 day strength). The interaction between calcination temperature and PG addition is also substantial, as evidenced by a steep response surface and relatively dense contour lines. In contrast, the response surface for PG addition and CS addition is relatively flat, with sparse contour lines, indicating a weaker influence on the response variable.

Fig. 18 Interactive effects of multiple variables on 3 day compressive strength ((a) temperature and addition amount of CS; (b) temperature and addition amount of PG; (c) addition amount of CS and PG).

These results suggest that, among the single variables, the order of influence on 3 day compressive strength is: calcination temperature > PG addition > CS addition. For multi-factor interactions, the order is: calcination temperature and PG addition > calcination temperature and CS addition > PG addition and CS addition.

3.3.2. 28 day compressive strength. Table 7 presents the ANOVA results for the response values of the 28 day compressive strength model. The results show that calcination temperature ($F = 55.41$) exerted the greatest influence on 28 day compressive strength, followed by CS addition ($F = 7.04$), while the effect of PG addition ($F = 1.35$) was comparatively weaker. The p-values for calcination temperature and CS addition were both less than 0.05, indicating statistically significant effects on 28 day compressive strength.

Fig. 19 illustrates the interactive effects of multiple variables on 28 day compressive strength. As shown in the figure, the 3D response surface for calcination temperature and CS addition is steep, with dense contour lines, indicating a pronounced effect. The surface for calcination temperature and PG addition is moderately steep with relatively dense contour lines, suggesting a decrease in the level of significance. In contrast, the response surface for PG addition and CS addition is flat, with sparse contour lines, indicating a weaker influence.
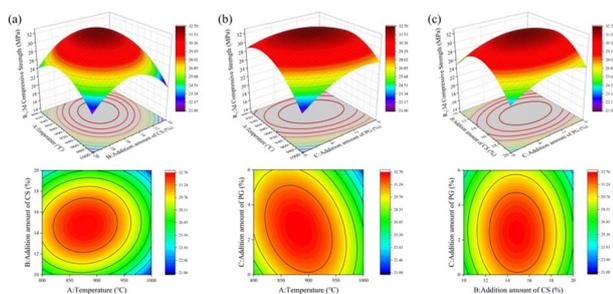
Table 7 ANOVA analysis of 28d compressive strength model of response value

| Source	Sum of squares	Degrees of freedom	Mean square	F-value	P-value	Significance
Model	144.03	9	16	21.99	0.0002	Highly significant
A	40.32	1	40.32	55.41	0.0001	Highly significant
B	5.12	1	5.12	7.04	0.0328	Significant
C	0.98	1	0.98	1.35	0.2839	Not significant
AB	38.25	1	38.25	52.57	0.0002	Highly significant
AC	8.32	1	8.32	11.44	0.0117	Significant
BC	2.77	1	2.77	3.81	0.0919	Not significant
A^2	27.22	1	27.22	37.41	0.0005	Highly significant
B^2	5.12	1	5.12	7.04	0.0328	Significant
C^2	11.5	1	11.5	15.81	0.0054	Highly significant
Residual	5.09	7	0.7277			
Lack of fit	3.79	3	1.26	3.88	0.1114	Not significant
Error	1.3	4	0.3254			
Total	149.12	16				
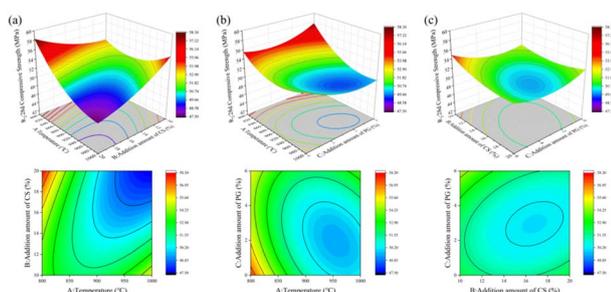
Fig. 19 Interactive effects of multiple variables on 28 day compressive strength ((a) temperature and addition amount of CS; (b) temperature and addition amount of PG; (c) addition amount of CS and PG).

In summary, the order of influence of single factors on 28 day compressive strength is: calcination temperature > CS addition > PG addition. For multi-factor interactions, the order is: calcination temperature and CS addition > calcination temperature and PG addition > PG addition and CS addition.

3.3.3. Optimization results and validation. MWCS paste replacing 30% of OPC was used for the compressive strength validation. Based on the response surface optimization, the maximum 3 day compressive strength was set as the optimization objective to establish the MWCS paste compressive strength model R1. The optimized mix proportions were: a calcination temperature of 882.45 °C, CS addition of 14.78%, and PG addition of 2.62%. The model predicted optimal results of 33.07 MPa for 3 day compressive strength and 52.79 MPa for 28 day compressive strength. According to the response surface optimization conditions, five parallel experiments were conducted to validate the model predictions, and the results are summarized in Table 8.

To address concerns regarding experimental errors in Table 8, all compressive strength tests were conducted in triplicate under identical curing and testing conditions, and the average value was calculated. The maximum deviation for the 3 day compressive strength was 2.87%, and for the 28 day compressive strength was 4.79%, both below the commonly accepted threshold of 5% for cement-based materials. This demonstrates that the reproducibility and reliability of the experimental

results are sufficient for scientific analysis and practical application, and that both R1 and R2 can effectively predict the 3 day and 28 day compressive strengths of MWCS paste replacing 30% of OPC.

3.4 Cost and carbon emissions

The production cost and carbon emissions of the optimized MWCS were calculated and analyzed. Prior to and after calcination, the raw materials were ground using an industrial ball mill (1000 kW) for 15 minutes and 5 minutes, respectively. The multi-solid waste composite SS was calcined for 175 minutes in an industrial calcination furnace (1750 kW). The unit cost and carbon emissions for each kilowatt hour of electricity were 0.7 RMB and 0.785 kg CO_2 e, respectively. The production cost and carbon emissions are shown in Table 9.

The economic and environmental benefits of MWCS were evaluated by comparison with the costs and carbon emissions of the material's traditional processing (MTP). As of January 2025, the price of OPC was 546 RMB per t, with carbon emissions of 735 kg CO_2 e per t.[51] The traditional processing costs for SS, CS, and PG were 300 RMB per t, 100 RMB per t, and 60 RMB per t, respectively, with carbon emissions of 500 kg CO_2 e per t, 20 kg CO_2 e per t, and 12 kg CO_2 e per t.

Fig. 20 compares the costs and carbon emissions between MTP and MWCS. Compared with MTP, the cost of MWCS was reduced from 342.94 RMB per t to 190.19 RMB per t, representing a 44.54% decrease. When replacing 30% OPC, the carbon emissions decreased from 748.88 kg CO_2 e per t to 529.17 kg CO_2 e per t, a reduction of 29.34%. The development and application of MWCS thus effectively reduce both the cost and carbon emissions compared to MTP.

4 Discussion

Although the chemical composition of municipal sewage sludge and solid wastes such as carbide slag and phosphogypsum may vary by region, the overall design logic of this study ensures broad applicability. Municipal sewage sludge typically exhibits high loss on ignition and contains abundant silico-aluminous

Table 8 Parallel test results

3 day compressive strength (MPa)	Mean 3 day compressive strength (MPa)	Deviation of 3 day compressive strength (%)	28 day compressive strength (MPa)	Mean 28 day compressive strength (MPa)	Deviation of 28 day compressive strength (%)
32.37	32.12	2.87	54.75	55.32	4.79
33.16			56.80		
32.15			55.81		
31.95			54.63		
31.17			54.59		

Table 9 Production cost and carbon emissions of the optimized MWCS

Materials	Cost (RMB per t)			Carbon emissions (kg CO_2 e per t)		
	Grinding	Calcination	Total	Grinding	Calcination	Total
SS	2.79	48.68	51.48	2.19	38.22	40.41
CS	0.09	1.54	1.63	0.07	1.21	1.28
PG	0.50	8.71	9.21	0.39	6.84	7.23

phases that can be transformed into reactive amorphous phases by calcination. Carbide slag is primarily introduced as a calcium-rich component to regulate the Ca/Si ratio and enhance the hydration activity of the silico-aluminous matrix. Phosphogypsum provides both calcium and sulfate ions, facilitating pH adjustment and the formation of ettringite and other hydration products. Therefore, the present research focuses on the effectiveness of Ca and S source regulation for activating the pozzolanic and cementitious properties of multi-solid waste composite calcined sewage sludge. The actual mix proportions can be flexibly optimized according to local raw material characteristics, while the fundamental mechanisms for Ca and S modulation remain universal and are validated in this work.

The composition and hydration performance of multi-solid waste composite calcined sewage sludge (MWCS) are primarily influenced by the following factors: (1) the relative content of calcium, silicon, aluminum, and sulfur in the raw materials, especially the Ca/Si and Ca/S ratios, which determine the formation of key hydration products; (2) the specific dosage and combination of each component (sewage sludge, carbide slag, and phosphogypsum), which modulate the balance and synergy of reactive species; and (3) the calcination temperature, which affects the extent of phase transformation and the generation of amorphous active phases. Adjusting the calcium content mainly regulates the pozzolanic activity and promotes the formation of calcium silicate and aluminate hydrates, while sulfate ions introduced by phosphogypsum influence the generation of ettringite and pore structure. These factors interact to determine the hydration mechanism and cementitious efficiency of MWCS, making the regulation strategy universally applicable to different types of industrial solid wastes.

The enhanced cementitious performance of MWCS is attributed to the synergistic chemical reactions among the silicon–aluminum phases in sewage sludge, calcium sources in carbide slag, and sulfate sources in phosphogypsum during high-temperature calcination. Specifically, the decomposition of kaolinite and muscovite in sludge generates amorphous silica and alumina, which react with calcium oxide (from CS) to form calcium silicate hydrate (C–S–H) and calcium aluminate phases. Meanwhile, the introduction of sulfate ions (from PG) facilitates the formation of ettringite (AFt), further optimizing the microstructure of the hydrated paste. These coupled reactions not only enhance the early and late strength development but also promote the densification of the pore structure, as demonstrated by XRD, FTIR, and NMR analyses. Thus, the regulation of calcium and sulfur components enables precise control of the hydration pathways and the optimization of cementitious properties.

5 Conclusion

In this study, CS and PG were co-calcined with SS at high temperatures. The hydration characteristics of calcined SS and
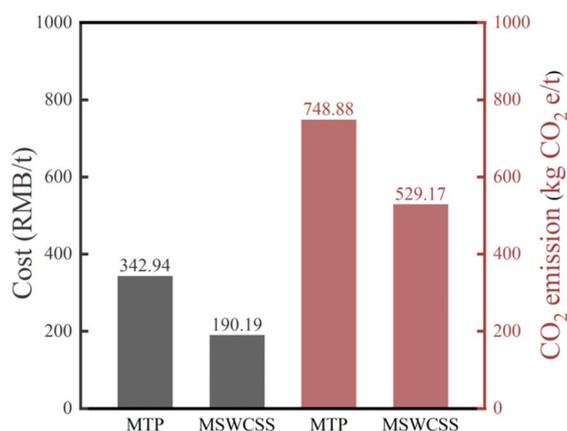

Fig. 20 Comparison of cost and carbon emissions.

its cement pastes were investigated using XRD, FTIR, T_2NMR, SEM, and TG-DSC. Response surface methodology was applied to optimize the MWCS mix proportions. The main conclusions are as follows:

(1) The crystalline structures of potentially pozzolanic minerals in SS, such as kaolinite and muscovite, were converted into amorphous phases after high-temperature calcination, thereby activating the pozzolanic reactivity of SS. As the calcination temperature increased from 800 °C to 1000 °C, this transformation diminished, indicating that 800 °C is the threshold temperature for effectively activating the pozzolanic potential of SS.

(2) The additions of CS and PG significantly influenced the cementitious properties of SS. XRD and FTIR analyses revealed that, at 30% CS addition or 15% PG addition, the amorphous reactive silica and alumina produced from the high-temperature decomposition of SS reacted optimally with the decomposition products of CS or PG, resulting in the best cementitious effect. The optimal reaction temperature was identified as 800 °C.

(3) When SS calcined at 800 °C was used to replace 30% of OPC in paste, both 3 day and 28 day compressive strengths were maximized. Microstructural analyses indicated that calcination at 800 °C imparted the highest pozzolanic activity to SS, promoting secondary hydration of CH in the paste. CS facilitated the formation of cementitious phases such as CA, while PG decomposition contributed to C_3S formation and enhanced its reactivity. These effects supported the generation of hydration products such as AFt and CH, ultimately reducing the pore size and porosity of the paste.

(4) Response surface methodology was used to evaluate the effects of single factors and their interactions on 3 day and 28 day compressive strengths, and to optimize the MWCS mix design. Calcination temperature had the greatest influence on both strengths, with PG addition mainly affecting 3 day strength and CS addition mainly affecting 28 day strength. Among interactions, calcination temperature combined with PG addition most impacted 3 day strength, while calcination temperature combined with CS addition most impacted 28 day strength. The optimal mix proportion was 882.45 °C, 14.78% CS, and 2.62% PG.

(5) The optimized MWCS achieved a production cost of 190.19 RMB per t and carbon emissions of 529.17 kg CO_2 e per t, representing reductions of 44.54% in cost and 29.34% in carbon emissions compared to conventional processes. The MWCS developed through thermal activation and synergistic utilization of multiple solid wastes exhibits remarkable economic and environmental advantages. The optimized MWCS can be used as a cementitious material for low-strength engineering applications or as a partial replacement for cement.

Data availability

The data are available from the corresponding author on reasonable request.

Author contributions

Juntao Ma: conceptualization, data curation, investigation, methodology, writing-original draft. Hao Zheng: writing-review & editing. Hao Qiu: methodology, writing-review & editing. Yunfei Tan: funding acquisition. Shunbo Zhao: methodology, supervision, review & editing; all authors have read and agreed to the published version of the manuscript.

Conflicts of interest

There are no conflicts to declare.

Acknowledgements

Notes and references

1 G. Giannopoulos, V. A. Tzanakakis, G. Duelli, I. Anastopoulos, V. G. Aschonitis, G. Arampatzis and P. E. Barouchas, Municipal sewage sludge treatment and soil pH conclusively affect the nitrogen dynamics of amended soils, *Environ. Adv.*, 2025, **19**, 100618, DOI: **10.1016/j.envadv.2025.100618**.

2 R. Ferrentino, M. Langone, L. Fiori and G. Andreottola, Full-scale sewage sludge reduction technologies: a review with a focus on energy consumption, *Water*, 2023, **15**(4), 615, DOI: **10.3390/w15040615**.

3 M. Bagheri, T. Bauer, L. E. Burgman and E. Wetterlund, Fifty years of sewage sludge management research: mapping researchers' motivations and concerns, *J. Environ. Manage.*, 2023, **325**, 116412, DOI: **10.1016/j.jenvman.2022.116412**.

4 M. Bagheri, T. Bauer, L. E. Burgman and E. Wetterlund, Fifty years of sewage sludge management research: mapping researchers' motivations and concerns, *J. Environ. Manage.*, 2023, **325**, 116412, DOI: **10.1016/j.cej.2017.12.149**.

5 Q. Zhang, J. Hu, D. J. Lee, Y. Chang and Y. J. Lee, Sludge treatment: current research trends, *Bioresour. Technol.*, 2017, **243**, 1159–1172, DOI: **10.1016/j.biortech.2017.07.070**.

6 N. Eshtiaghi, F. Markis, S. D. Yap, J. C. Baudez and P. Slatter, Rheological characterisation of municipal sludge: a review, *Water Res.*, 2013, **47**(15), 5493–5510, DOI: **10.1016/j.watres.2013.07.001**.

7 S. Li, C. Li and Z. Shao, Microwave pyrolysis of sludge: a review, *Sustain. Environ. Res.*, 2022, **32**(1), 23, DOI: **10.1186/s42834-022-00132-z**.

8 Y. Liu, J. Zhou, S. Lu and J. Ren, Towards the new era of sewage sludge management in China: status, challenges, and perspectives, *Process Saf. Environ. Prot.*, 2025, **167**, 107201, DOI: **10.1016/j.psep.2025.107201**.

9 W. Zhang, Q. Dai, X. Yang, W. Gao, S. Zhao, P. Yu and D. Wang, Odor characteristics of wastewater treatment

plant sludge during treatment and disposal and emission reduction control measures: a short review, *Chin. J. Environ. Eng.*, 2023, **17**(2), 1–18, DOI: **10.12030/j.cjee.202203007**.

10 Y. Yang, J. Luan, J. Nie, X. Zhang, J. Du, G. Zhao and Y. Li, Reprocessing and resource utilization of landfill sludge: a case study in a Chinese megacity, *Water*, 2024, **16**(3), 468, DOI: **10.3390/w16030468**.

11 S. R. Meda, S. K. Sharma and G. D. Tyagi, Utilization of waste sludge as a construction material: a review, *Mater. Today Proc.*, 2021, **46**, 4195–4202, DOI: **10.1016/j.matpr.2021.02.762**.

12 K. Taki, S. Choudhary, S. Gupta and M. Kumar, Enhancement of geotechnical properties of municipal sewage sludge for sustainable utilization as engineering construction material, *J. Clean. Prod.*, 2020, **251**, 119723, DOI: **10.1016/j.jclepro.2019.119723**.

13 M. Hasan, M. T. Al Biruni, A. Afia and T. Ahmed, Utilization of sludge from water treatment plant as a filler material in pavements, *J. Mater. Cycles Waste Manag.*, 2022, **24**(6), 2656–2668, DOI: **10.1007/s10163-022-01505-7**.

14 S. Thukkaram and A. A. Kumar, Characteristics of sewage sludge and its potential applications in the construction industry: a review, *Int. J. Environ. Waste Manag.*, 2021, **28**(1), 17–40, DOI: **10.1504/IJEWM.2021.117007**.

15 T. Zat, M. Bandieira, N. Sattler, A. M. Segadães, R. C. Cruz, G. Mohamad and E. D. Rodríguez, Potential re-use of sewage sludge as a raw material in the production of eco-friendly bricks, *J. Environ. Manage.*, 2021, **297**, 113238, DOI: **10.1016/j.jenvman.2021.113238**.

16 J. B. da Silva, T. Zat, E. S. Werner, F. A. Brehm, J. P. Gonçalves, M. T. Souza and E. D. Rodríguez, Recycling of municipal sewage sludge from Brazilian wastewater treatment plants for the manufacture of environmentally friendly ceramic bricks, *Case Stud. Constr. Mater.*, 2024, **21**, e03610, DOI: **10.1016/j.cscm.2024.e03610**.

17 J. B. da Silva, T. Zat, E. S. Werner, F. A. Brehm, J. P. Gonçalves, M. T. Souza and E. D. Rodríguez, Recycling of municipal sewage sludge from Brazilian wastewater treatment plants for the manufacture of environmentally friendly ceramic bricks, *Case Stud. Constr. Mater.*, 2024, **21**, e03610, DOI: **10.1016/j.conbuildmat.2015.08.122**.

18 C. O. Rusănescu, G. Voicu, G. Paraschiv, M. Begea, L. Purdea, I. C. Petre and E. V. Stoian, Recovery of sewage sludge in the cement industry, *Energies*, 2022, **15**(7), 2664, DOI: **10.3390/en15072664**.

19 E. Twagirayezu, L. Fan, X. Liu, A. Iqbal, X. Lu, X. Wu and F. Zan, Comparative life cycle assessment of sewage sludge treatment in Wuhan, China: sustainability evaluation and potential implications, *Sci. Total Environ.*, 2024, **913**, 169686, DOI: **10.1016/j.scitotenv.2023.169686**.

20 A. H. Khan, A. Firoozi, P. Alam, I. S. Agwa, C. Rahmawati and M. A. Hasan, Supplementary cementitious materials: recent developments, performance insights and potential applicability, *Front. Mater.*, 2025, **12**, 1608358, DOI: **10.3389/fmats.2025.1608358**.

21 T. Mi, Y. Li, E. H. Yang and C. Unluer, Use of sludge produced from reject brine as a supplementary cementitious material with enhanced carbonation capability, *Cem. Concr. Compos.*, 2025, **160**, 10605, DOI: **10.1016/j.cemconcomp.2025.106051**.

22 M. Mottakin, S. D. Datta, M. M. Hossain, M. H. R. Sobuz, S. A. Rahman and M. Alharthai, Evaluation of textile effluent treatment plant sludge as supplementary cementitious material in concrete using experimental and machine learning approaches, *J. Build. Eng.*, 2024, **96**, 110627, DOI: **10.1016/j.jobe.2024.110627**.

23 M. A. Mosaberpanah, S. B. Olabimtan, A. P. Balkis, B. O. Rabiu, B. O. Oluwole and C. S. Ajuonuma, Effect of biochar and sewage sludge ash as partial replacement for cement in cementitious composites: mechanical and durability properties, *Sustainability*, 2024, **16**(4), 1522, DOI: **10.3390/su16041522**.

24 J. A. Bogas, A. Carrico and A. J. Tenza-Abril, Microstructure of thermoactivated recycled cement pastes, *Cem. Concr. Res.*, 2020, **138**, 106226, DOI: **10.1016/j.cemconres.2020.106226**.

25 J. Wang, M. Mu and Y. Liu, Recycled cement, *Constr. Build. Mater.*, 2018, **190**, 1124–1132, DOI: **10.1016/j.conbuildmat.2018.09.181**.

26 R. Serpell and F. Zunino, Recycling of hydrated cement pastes by synthesis of α' H-C2S, *Cem. Concr. Res.*, 2017, **100**, 398–412, DOI: **10.1016/j.cemconres.2017.08.001**.

27 M. A. Tantawy, Characterization and pozzolanic properties of calcined alum sludge, *Mater. Res. Bull.*, 2015, **61**, 415–421, DOI: **10.1016/j.materresbull.2014.10.042**.

28 Q. Jia, Y. Zhuge, W. Duan, *et al.*, Valorisation of alum sludge to produce green and durable mortar, *Waste Dispos. Sustain. Energy*, 2022, **4**, 283–295, DOI: **10.1007/s42768-022-00113-3**.

29 Z. Chang, G. Long, Y. Xie and J. L. Zhou, Pozzolanic reactivity of aluminum-rich sewage sludge ash: Influence of calcination process and effect of calcination products on cement hydration, *Constr. Build. Mater.*, 2022, **318**, 126096, DOI: **10.1016/j.conbuildmat.2021.126096**.

30 I. V. Fernandes, V. M. Lima, C. F. Nascimento, H. G. Carvalho, C. L. Santos and A. A. M. Neto, Valorization of textile sludge for use as supplementary cementitious material: benefiting processes, pozzolanic activity, and application in no-slump concrete, *Constr. Build. Mater.*, 2025, **458**, 139619, DOI: **10.1016/j.conbuildmat.2024.139619**.

31 M. A. Aranda, I. Artioli, T. Bier, À. G. De la Torre, D. Freyer, R. Kaden, *et al. Cementitious Materials: Composition, Properties, Application*, Walter de Gruyter GmbH & Co KG, Berlin, 2017.

32 M. E. Shabab, K. Shahzada, B. Gencturk, M. Ashraf and M. Fahad, Synergistic effect of fly ash and bentonite as partial replacement of cement in mass concrete, *KSCE J. Civ. Eng.*, 2016, **20**(5), 1987–1995, DOI: **10.1007/s12205-015-0166-x**.

33 J. Zhang, S. Li and Z. Li, Investigation of the synergistic effects in quaternary binder containing red mud, blast furnace slag, steel slag and flue gas desulfurization

gypsum based on artificial neural networks, *J. Clean. Prod.*, 2020, **273**, 122972, DOI: **10.1016/j.jclepro.2020.122972**.

34 C. Sun, J. Zhang, C. Yan, L. Yin, X. Wang and S. Liu, Hydration characteristics of low carbon cementitious materials with multiple solid wastes, *Constr. Build. Mater.*, 2022, **322**, 126366, DOI: **10.1016/j.conbuildmat.2022.126366**.

35 D. Duan, H. Liao, F. Wei, J. Wang, J. Wu and F. Cheng, Solid waste-based dry-mix mortar using fly ash, carbide slag, and flue gas desulfurization gypsum, *J. Mater. Res. Technol.*, 2022, **21**, 3636–3649, DOI: **10.1016/j.jmrt.2022.10.157**.

36 X. Gu, X. Ge, J. Liu, G. Song, S. Wang, Z. Hu and H. Wang, Study on the synergistic effect of calcium carbide residue-fly ash enhanced desulphurisation gypsum under high temperature maintenance condition, *Constr. Build. Mater.*, 2024, **412**, 134706, DOI: **10.1016/j.conbuildmat.2023.134706**.

37 C. Ren, W. Wang and G. Li, Preparation of high-performance cementitious materials from industrial solid waste, *Constr. Build. Mater.*, 2017, **152**, 39–47, DOI: **10.1016/j.conbuildmat.2017.06.124**.

38 D. Su, G. Yue, Q. Li, Y. Guo, S. Gao and L. Wang, Research on the preparation and properties of high belite sulphoaluminate cement based on various industrial solid wastes, *Materials*, 2019, **12**(9), 1510, DOI: **10.3390/ma12091510**.

39 G. E. P. Box and D. W. Behnken, Some new three-level designs for the study of quantitative variables, *Technometrics*, 1960, **2**(4), 455–475, DOI: **10.1080/00401706.1960.10489912**.

40 W. A. Jensen, Response surface methodology: process and product optimization using designed experiments, *J. Qual. Technol.*, 2017, **49**(2), 140–142, DOI: **10.1080/00224065.2017.11917988**.

41 Standardization Administration of China, *Test Method for Strength of Cement Mortar (ISO Method), GB/T 17671-1999*, China Standards Press, Beijing, 1999.

42 S. Scherb, N. Beuntner and K. C. Thienel, Reaction kinetics of basic clay components present in natural mixed clays, in *Calcined Clays for Sustainable Concrete*, Springer, Dordrecht, 2017, pp. 427–433, DOI: **10.1007/978-94-024-1207-9_69**.

43 F. Engström, D. Adolfsson, C. Samuelsson, Å. Sandström and B. Björkman, A study of the solubility of pure slag minerals, *Miner. Eng.*, 2013, **41**, 46–52, DOI: **10.1016/j.mineng.2012.10.004**.

44 T. M. Agra, V. M. Lima, P. E. Basto and A. A. M. Neto, Characterizing and processing a kaolinite-rich water treatment sludge for use as high-reactivity pozzolan in cement manufacturing, *Appl. Clay Sci.*, 2023, **236**, 106870, DOI: **10.1016/j.clay.2023.106870**.

45 T. Hemalatha, M. Mapa, N. George and S. Sasmal, Physico-chemical and mechanical characterization of high volume fly ash incorporated and engineered cement system towards developing greener cement, *J. Clean. Prod.*, 2016, **125**, 268–281, DOI: **10.1016/j.jclepro.2016.03.118**.

46 J. Yang, Y. Ren, S. Chen, Z. Zhang, H. Pang, X. Wang and J. Lu, Thermally activated drinking water treatment sludge as a supplementary cementitious material: properties,

47 P. de Azevedo Basto, H. S. Junior and A. A. de Melo Neto, Characterization and pozzolanic properties of sewage sludge ashes by electrical conductivity, *Cem. Concr. Compos.*, 2019, **104**, 10341010, DOI: **10.1016/j.cemconcomp.2019.103410**.

48 X. Wang, N. Wen, J. Liu, S. Zhang, H. Michael and P. Rodrigo, Carbonation of steel slag and gypsum for building materials and associated reaction mechanisms, *Cem. Concr. Res.*, 2019, **125**, 105893, DOI: **10.1016/J.CEMCONRES.2019.105893**.

49 Y. B. Teng, S. H. Liu, Z. C. Zhang, *et al.*, Effect of triethanolamine on the chloride binding capacity of cement paste with a high volume of fly ash, *Constr. Build. Mater.*, 2022, **315**, 125612, DOI: **10.1016/j.conbuildmat.2021.125612**.

50 E. O. Fridjonsson, A. Hasan, A. B. Fourie and M. L. Johns, Pore structure in a gold mine cemented paste backfill, *Miner. Eng.*, 2013, **53**, 144–151, DOI: **10.1016/j.mineng.2013.07.017**.

51 M. Gou, W. Hou, L. Zhou, J. Zhao and M. Zhao, Preparation and properties of calcium aluminate cement with Bayer red mud, *Constr. Build. Mater.*, 2023, **373**, 130827, DOI: **10.1016/j.conbuildmat.2023.130827**.

52 W. Lou, B. Guan and Z. Wu, Calorimetric study of ternary binder of calcium aluminate cement, Portland-limestone cement and FGD gypsum, *J. Therm. Anal. Calorim.*, 2010, **101**(1), 119–127, DOI: **10.1007/s10973-009-0542-1**.

53 J. Bizzozero, C. Gosselin and K. L. Scrivener, Expansion mechanisms in calcium aluminate and sulfoaluminate systems with calcium sulfate, *Cem. Concr. Res.*, 2014, **56**, 190–202, DOI: **10.1016/j.cemconres.2013.11.011**.

54 J. Bizzozero, C. Gosselin and K. L. Scrivener, Expansion mechanisms in calcium aluminate and sulfoaluminate systems with calcium sulfate, *Cem. Concr. Res.*, 2014, **56**, 190–202, DOI: **10.1016/j.conbuildmat.2022.128398**.

55 M. Zhang, M. Zhao, G. Zhang, J. M. Sietins, S. Granados-Focil, M. S. Pepi and M. Tao, Reaction kinetics of red mud-fly ash based geopolymers: effects of curing temperature on chemical bonding, porosity, and mechanical strength, *Cem. Concr. Compos.*, 2018, **93**, 175–185, DOI: **10.1016/j.cemconcomp.2018.07.008**.

56 X. Chen, S. Li, W. Chen, Y. Chen, H. Chen and H. Yang, Influence of calcination temperature on calcined carbide slag assisted biomass pyrolysis, *Fuel Process. Technol.*, 2022, **234**, 107339, DOI: **10.1016/j.fuproc.2022.107339**.

57 J. Zhang, C. Li, T. Lv, Q. Zhao and B. Dong, Microstructure regulation and performance enhancement of waste gypsum-based supersulfated cement with sintered sludge ash, *Constr. Build. Mater.*, 2025, **477**, 141358, DOI: **10.1016/j.conbuildmat.2025.14135**.

58 L. Dvorkin, V. Zhitkovsky, I. Hager, T. Tracz and T. Zdeb, Structure formation and properties of activated supersulfate cement, *Materials*, 2025, **18**(9), 1912, DOI: **10.3390/ma18091912**.

59 T. Jiang, K. Cui and J. Chang, Development of low-carbon cement: Carbonation of compounded C2S by β-C_2S and γ-C_2S, *Cem. Concr. Compos.*, 2023, **139**, 105071, DOI: **10.1016/j.cemconcomp.2023.105071**.

60 T. Staněk, M. Boháč and P. Sulovský, Chemical activation of dicalcium silicate and its use for cement production, *Adv. Mater. Res.*, 2019, **1151**, 17–21, DOI: **10.4028/www.scientific.net/AMR.1151.17**.

61 Q. Song, M. Z. Guo, L. Wang and T. C. Ling, Use of steel slag as sustainable construction materials: a review of accelerated carbonation treatment, *Resour. Conserv. Recycl.*, 2021, **173**, 105740, DOI: **10.1016/J.RESCONREC.2021.105740**.

62 S. J. S. Chelladurai, K. Murugan, A. P. Ray, M. Upadhyaya, V. Narasimharaj and S. Gnanasekaran, Optimization of process parameters using response surface methodology: a review, *Mater. Today Proc.*, 2021, **37**, 1301–1304, DOI: **10.1016/j.matpr.2020.06.466**.

63 Z. Li, D. Lu and X. Gao, Optimization of mixture proportions by statistical experimental design using response surface method: a review, *J. Build. Eng.*, 2021, **36**, 10210, DOI: **10.1016/j.jobe.2020.102101**.

64 A. I. Khuri and S. Mukhopadhyay, Response surface methodology, *WIREs Comput. Stat.*, 2010, **2**(2), 128–14, DOI: **10.1002/wics.73**.

65 R. F. Gunst, Response surface methodology: process and product optimization using designed experiments, *Technometrics*, 1996, **38**(3), 284–286, DOI: **10.1080/00401706.1996.10484509**.